ARTICLES

Journal of Semiconductors
(2020) 41, 122501
doi: 10.1088/1674-4926/41/12/122501

Prediction and observation of defect-induced room-temperature ferromagnetism in halide perovskites

Zhiguo Sun[1], Bo Cai[1], Xi Chen[1, †], Wenxian Wei[2], Xiaoming Li[1], Dandan Yang[1], Cuifang Meng[1], Ye Wu[1], and Haibo Zeng[1, †]

[1]MIIT Key Laboratory of Advanced Display Materials and Devices, Institute of Optoelectronics & Nanomaterials, College of Materials Science and Engineering, Nanjing University of Science and Technology, Nanjing 210094, China

[2]Testing Center, Yangzhou University, Yangzhou 225009, China

Abstract: The possibility to induce a macroscopic magnetic moment in lead halide perovskites (LHPs), combined with their excellent optoelectronic properties, is of fundamental interest and has promising spintronic applications. However, these possibilities remain an open question in both theory and experiment. Here, theoretical and experimental studies are performed to explore ferromagnetic states in LHPs originated from lattice defects. First-principle calculations reveal that shallow-level Br vacancies in defective $CsPbBr_3$ can produce spin-splitting states and the coupling between them leads to a ferromagnetic ground state. Experimentally, ferromagnetism at 300 K is observed in room-temperature synthesized $CsPbBr_3$ nanocrystals, but is not observed in hot-injection prepared $CsPbBr_3$ quantum dots and in $CsPbBr_3$ single crystals, highlighting the significance played by vacancy defects. Furthermore, the ferromagnetism in the $CsPbBr_3$ nanocrystals can be enhanced fourfold with Ni^{2+} ion dopants, due to enhancement of the exchange coupling between magnetic polarons. Room-temperature ferromagnetism is also observed in other LHPs, which suggests that vacancy-induced ferromagnetism may be a universal feature of solution-processed LHPs, which is useful for future spintronic devices.

Key words: lead halide perovskites; magnetic nanocrystals; halogen vacancy defects; DFT calculations; magnetic polarons

Citation: Z G Sun, B Cai, X Chen, W X Wei, X M Li, D D Yang, C F Meng, Y Wu, and H B Zeng, Prediction and observation of defect-induced room-temperature ferromagnetism in halide perovskites[J]. *J. Semicond.*, 2020, 41(12), 122501. http://doi.org/10.1088/1674-4926/41/12/122501

1. Introduction

Modern logic and memory devices work through electrical control of n- or p-type charge carriers in semiconductor transistors. However, their further miniaturization has reached a bottleneck due to the quantum tunneling effect and also due to energy-consumption issues. Making use of another property of electrons (*i.e.*, the spin property) to develop semiconductor spintronic devices is key to overcome these barriers[1] because electrically manipulating spin is more both energy-efficient and faster than controlling charge. To this end, many theoretical and experimental studies have been conducted in the last two decades to attempt to discover room-temperature (RT) ferromagnetic semiconductors[2], as producing long-range spin ordering (ferromagnetism) in semiconductors is the first step to constructing spintronic devices. Because natural ferromagnetic semiconductors are rare, RT ferromagnetic semiconductors are initially created by artificially doping nonmagnetic wide band-gap metal oxides or nitrides (*e.g.*, ZnO, TiO_2, SnO_2, CeO_2, and GaN) with magnetic 3*d* transition metal (TM) atoms (*e.g.*, Mn, Fe, Co, or Cu)[3–7]. Soon after, it was found that many semiconductors, including the above-mentioned ones, could show RT ferromagnetism, even without any magnetic dopants. This phenomenon was termed d^0 ferromagnetism, to underline the absence of partially-filled *d* or *f* orbitals in the semiconductors[8, 9]. Experimental evidence has suggested that d^0 ferromagnetism is strongly correlated to vacancy defects in crystals[10–13]. Theoretical studies have revealed that both cation and anion vacancy defects can produce local spin moments by breaking the symmetry of spin structures, and the exchange coupling between the vacancy spins gives rise to the d^0 ferromagnetism[14–17]. Given the inevitability of growth-related vacancy defects in real crystals, vacancy-induced d^0 ferromagnetism may have congenital advantages for designing semiconductor spintronic devices.

However, there is an increasing number of studies which have reported that the vacancy defects that are responsible for the d^0 ferromagnetism; for example, the oxygen vacancy in ZnO, TiO_2, and SnO_2, the zinc and titanium vacancies in ZnO and TiO_2, and the gallium vacancy in GaN are deep in energy levels[18–21]. It is known that deep-level defects typically act as carrier recombination centers, and therefore they should be eliminated to avoid degradation in semiconductor performance. This conflicts with the theory of vacancy-induced d^0 ferromagnetism, which requires a considerable number of vacancies to develop long-range exchange coupling, and thus hampers d^0 ferromagnetism in future applications. From this point of view, it is highly desirable to produce d^0 ferromagnetism in a semiconductor host that is tolerant of defects.

Recently, a class of lead halide perovskite (LHP) semiconductors with the chemical formula ABX_3 (A = Cs^+, $CH_3NH_3^+$ *et*

Correspondence to: X Chen, xichen@njust.edu.cn; H B Zeng, zeng.haibo@njust.edu.cn

Received 19 APRIL 2020; Revised 22 MAY 2020.

al., B = Pb^{2+}, and X = Cl^-, Br^-, or I^-) has attracted extensive studies in the fields of photovoltaics and optoelectronics[22]. These materials are commonly synthesized via solution processing methods, and thus often contain an ultrahigh thermal vacancy equilibrium concentration, typically at percent level[23]. Nevertheless, LHPs show impressive performances, such as ultralong carrier diffusion lengths[24], near-unit photoluminescence quantum yields[25], and efficiencies above 20% in solar cells and light-emitting devices[26–28]. These attributes indicate that the electrical and optical properties of LHPs have a high defect tolerance. Theoretical studies have suggested that these outstanding performances are helped by a special property that the predominating lattice defects in LHPs (*i.e.*, the halide vacancy) is in shallow energy levels[29, 30]. Furthermore, LHPs have large spin-orbit coupling, due to them containing Pb, which is a heavy element. A number of spin-orbit related phenomena, such as large Rashba spin splitting, field-induced spin polarization, and spin-to-charge current conversion, have been recently demonstrated in LHPs[31–34]. These phenomena suggest that LHPs have potential for spintronic applications. Therefore, it is highly interesting to explore whether the shallow-level halide vacancies in LHPs can produce ferromagnetism, which is critical for future spintronic applications. This question is yet to be studied, either from an experimental or a theoretical viewpoint.

Here, we demonstrate, through both theoretical and experimental approaches, that even without partially-filled *d* or *f* orbitals, defective LHPs can show ferromagnetic states, due to their lifted spin degeneracy by halogen vacancy. The vacancy-induced d^0 ferromagnetism is robust at RT, and can be improved by incorporating a tiny fraction of 3*d* ions into Pb sites. Our results may boost LHPs with excellent optical properties for applications in novel spintronic devices, such as spin light-emitting diodes and spin field-effect transistors.

2. Experimental section

2.1. Materials

$PbBr_2$ (99.99%), CsBr (99.5%), $PbCl_2$ (99.99%), PbI_2 (99.9%), CsCl (99.99%), CsI (99.9%), manganese(II) acetylacetonate [$Mn(acac)_2$, 97%], $Fe(acac)_2$ (98%), $Co(acac)_2$ (99%), $Ni(acac)_2$ (96%), $Cu(acac)_2$ (99%), $Zn(acac)_2$ (98%), hydrobromic acid (HBr, 40%), hydroiodic acid (HI, 47%), hydrochloric acid (HCl, 36.5%), 1-octadecene (ODE, 90%), and diethyl ether were purchased from Macklin. Cs_2CO_3 (99.99%), oleylamine (OAm, 90%), oleic acid (OA, 85%), dimethylsulfoxide (DMSO, 99.8%), methanol (MeOH, 99.9%), ethyl acetate (99%), and dimethylformamide (DMF, 99.9%) were purchased from Aladdin. Toluene (99.5%) was purchased from Sinopharm Chemical Reagent Corp., China. Methylammonium bromide (MABr, 99.5%) was purchased from Xi'an Polymer Light Technology Corp., China. All materials were used without further purification.

2.2. Preparation of OAmBr (Cl or I)

We take OAmBr as an example to show how OAmBr (Cl or I) was made. OAmBr was synthesized by reaction of the OAm with HBr. 20 mmol OAm in absolute ethanol was stirred and cooled in ice-bath, and then 20 mmol HBr was added drop by drop. The reaction solution was stirred for 12 h until all OAm was reacted. Then rotary evaporation was applied to obtain OAmBr pulp at 70 °C. After three times washing with diethyl ether, white powder was obtained and dried under vacuum at 40 °C overnight for future use. Similarly, OAmCl and OAmI were synthesized by reaction of the OAm with HCl and HI, respectively.

2.3. Synthesis and surface passivation of pure and 3*d* ion-doped LHPs at room temperature

We take $CsPbBr_3$ as an example to show how LHPs were made. Firstly, a mixture of $PbBr_2$ (1.2 mmol), CsBr (1.0 mmol), and $Ni(acac)_2$ at a designated Ni/Pb molar ratio from 0 to 20 mol% were dissolved in dimethylsulfoxide (DMSO, 10 mL). The insoluble residues were removed by using a filter with 22 μm pore size, and then the precursor solution was obtained. Next, oleylammonium (OAm, 20 μL), oleic acid (OA, 20 μL), and the precursor solution (0.2 mL) were then loaded into a 20 mL vial. Then, toluene (15 mL) was quickly added into the vial under vigorous stirring. After 5 min, the solution was centrifuged by 8000 rpm and then $CsPbBr_3$ nanocrystals were obtained. Finally, the obtained nanocrystals were washed by 8 mL toluene twice. After washing, the nanocrystals were redispersed in 4 mL toluene for further use. OAmBr (0.025 mg/mL) was added into the toluene-dispersed nanocrystals to situ passivate the nanocrystal surfaces. The whole synthetic process was carried out at room temperature.

2.4. Preparation of Cs-oleate

Cs_2CO_3 (0.36 g), OA (1.5 mL) and ODE (15 mL) were added to a 100 mL three-neck round-bottom flask and degassed under an Ar flow at room temperature for 15 min, and then heated at 120 °C under an Ar flow with constant stirring for 15 min to remove the moisture from the raw materials. Thereafter, the mixture was heated to 150 °C for 15 min under an Ar flow with constant stirring and lowered to 110 °C until further use.

2.5. Synthesis of pure and 3*d* ion-doped LHPs via hot-injection

We take $CsPbBr_3$ as an example to show how hot-injection LHPs were made. A mixture of 0.54 mmol of $PbBr_2$, $Ni(acac)_2$ at a designated Ni/Pb mole ratio from 0 to 20 mol% and 15 mL of ODE, 1.5 mL of OA, 1.5 mL of OAm was first added to a 100 mL three-neck flask, dried under vacuum for 1 h at 120 °C with constant stirring to remove the moisture from the raw materials, and then heated at 120 °C under a Ar flow. After 5 min, the mixture was heated to 170 °C, the Cs-oleate precursor (1.5 mL) were subsequently quickly injected. After reacting for 5 s, the reaction mixture was cooled to 20 °C rapidly by using an ice-water bath. The obtained quantum dots were inject 40 mL ethyl acetate collected by centrifugation at 10 000 rpm for 1 min.

2.6. Preparation of precursors for single crystal growth

2 mmol CsBr and 3 mmol $PbBr_2$ were dissolved by 5 mL DMSO with continuous stirring for 1 h at room temperature. Then, the solution was filtered using 45 μm-sized filter to remove the precipitate, and clear solution was obtained. After that, MeOH was titrated into the clear solution until the orange precipitates no longer dissolved. Finally, the orange precipitates were filtered and the clear precursor was collected for further crystal growth.

2.7. Growth of $CsPbBr_3$ single crystals

$CsPbBr_3$ single crystals were grown by the antisolvent

vapor-assisted crystallization method. About 10 mL clear precursors obtained above were put in a 20 mL container, and 15 mL MeOH was then added into an outer petri dish before sealing. MeOH was volatilized from the outer container to the inner one, forming saffron yellow $CsPbBr_3$ crystals. This growing process took 2 days. Finally, the obtained $CsPbBr_3$ crystals were washed with 110 °C DMF solution to remove the precursors attached to the crystal surfaces.

2.8. Composition, structural, magnetic, and optical characterizations

The real molar ratios of TM ions relative to Pb in TM-doped $CsPbBr_3$ were determined by using an inductively coupled plasma mass spectrometry (iCAP TQ, Thermo Scientific). The crystalline structures were characterized by powder X-ray diffraction (Bruker-AXS D8 Advance). The microstructure was characterized by using a Tecnai G20 transmission electron microscopy with operation voltage of 200 kV. The samples used for magnetic properties measurements were dried in a vacuum drying oven at vacuum of 2×10^{-2} Pa and at temperature of 40 °C. Then, the obtained powders were loaded into a capsule, and the magnetic properties were measured using a physical property measurement system (Quantum Design). The elemental valence states were investigated using an X-ray photoelectron spectrometer (Thermo Scientific ESCALAB 250Xi). Before recording the spectra, the surface contaminants of samples were removed by Ar ion etching with etching time of 60 s. To eliminate the charge effect, all binding energies were calibrated by the C 1*s* line at 284.6 eV. The electron spin resonance was carried out on a JEOL FA-200 instrument at X-band. The photoluminescence spectra were detected on Varian Cary Eclipse instrument.

2.9. First-principle calculation details

The theoretical derivation was carried out using first-principle density functional theory implemented in the Vienna Ab-initio Simulation Package (VASP)[35]. Geometry optimization and electronic structure calculations were carried out under the PBESOL exchange-correlation functional[36]. A kinetic energy cutoff of 500 eV was set on a grid of $5 \times 5 \times 5$ *k*-points for cubic $CsPbBr_3$ unit cell. The maximum force, maximum stress and maximum displacement are set to 0.01 eV/Å, 0.02 GPa and 5.0×10^{-4} Å, respectively. The lattice constant for a perfect cubic-phase $CsPbBr_3$ unit cell was optimized to be 5.80 Å. A single positively charged Br vacancy was introduced by removing one Br atom, and overall charge neutrality was achieved via a compensating background charge. Spin-orbit coupling was not considered here.

3. Results

3.1. Structural and optical properties characterizations

Before showing the magnetic results, we would like to present some structural and optical characterizations of Ni-doped $CsPbBr_3$ as a representative. The samples are named as $CsPb_{1-x}Ni_xBr_3$, where x is the real molar ratio of Ni relative to Pb, as determined from inductively coupled plasma mass spectrometry (Table S1, Supporting Information), and $x = 0$ represents pure $CsPbBr_3$. The samples were synthesized at RT through solution processing (see Experimental section). Figs. 1(a) and 1(b) display high-resolution transmission electron microscopy (TEM) images of $CsPb_{1-x}Ni_xBr_3$ with $x = 0$ and 0.31%, respectively. Clear lattice fringes can be observed, indicating that our samples are well crystalized. The fringe spacing determined by using fast Fourier transform patterns was found to be 0.5765 nm for both samples, which we attribute to the (100) plane. The low-resolution TEM images shown in insets reveal that both samples have typical square nanocrystal morphology, with an average size of ~ 55.2 nm. Fig. 1(c) shows X-ray diffraction (XRD) patters of $CsPb_{1-x}Ni_xBr_3$ with different x values. All samples can be indexed as $CsPbBr_3$ with cubic-phase structure. Close examination of the XRD patterns near $2\theta = 21.5°$ reveals that the Bragg angle θ shifted slightly but systematically to higher positions as x increased, suggesting that the lattice shrank. Fig. 1(d) shows the X-ray photoelectron spectrum of the Ni 2*p* level in $CsPb_{1-x}Ni_xBr_3$ with x = 0.31%. The peak located at around 855.42 eV is assigned to the Ni^{2+} $2p_{3/2}$ level. As the ion radius of Ni^{2+} (~0.83 Å for an octahedral site) is smaller than that of Pb^{2+} (~0.1 Å for an octahedral site), the lattice shrink confirms that the Ni^{2+} dopants were incorporated into the Pb^{2+} sites. Fig. 1(e) shows normalized photoluminescence spectra of $CsPb_{1-x}Ni_xBr_3$ nanocrystals with different x values measured at RT. The optical gap (*i.e.*, the energy value at the photoluminescence peak) was 2.4 eV for $x = 0$, which exhibits a slight red-shift with increasing x.

We adopted electron spin resonance (ESR, also known as electron paramagnetic resonance) to determine the type of defects that is predominant in our samples, as ESR is a defect-sensitive technique that is widely used to study defect physics. Fig. 1(f) shows the ESR first derivative signals as a function of the external magnetic field (H_{ext}), obtained from $CsPb_{1-x}Ni_xBr_3$ nanocrystals with $x = 0$ and 0.31% at RT. The two samples had the same weight (10.2 mg) for these ESR measurements. We can see that, although they are weak, clear resonance signals can be observed. Both samples exhibit the same resonance peak, same line shape, and same line width, indicating that the signals share the same origin. Using the formula $g = h\gamma/\mu_B H_{ext}$, where h is the Planck's constant, γ is the microwave frequency (9.85 GHz), and μ_B is the Bohr magnetron, the g factor was calculated to be 2.0033 for both samples, which can be assigned to the Br vacancy (V_{Br}) donor defect[37]. The value of the calculated g factor is very close to that of the free electron (2.0023), indicating that the donor electron is loosely bound to V_{Br}. This means that V_{Br} is in a shallow energy level, consistent with previous theoretical calculations[29, 30]. Given the relatively low formation energy among all possible type defect in LHPs (*i.e.*, vacancy defect, interstitial defect, and antisite defect)[23, 29, 30], we conclude that shallow-level V_{Br} was the predominant defect in our samples. Note that the peak intensity of the signals was almost the same for the two samples, indicating that the V_{Br} concentration varies not much in the undoped and doped $CsPbBr_3$.

3.2. First-principle prediction of vacancy-induced magnetism

We next elucidated the defect-induced magnetic states in $CsPbBr_3$ through first-principle density functional theory (DFT) calculations. Based on the above ESR results, we focused only on V_{Br} and its effects on the electronic structures of $CsPbBr_3$. Fig. 2(a) shows the perfect $3 \times 3 \times 3$ cubic-phase $CsPbBr_3$ supercells (left-hand column) used in the DFT calcula-

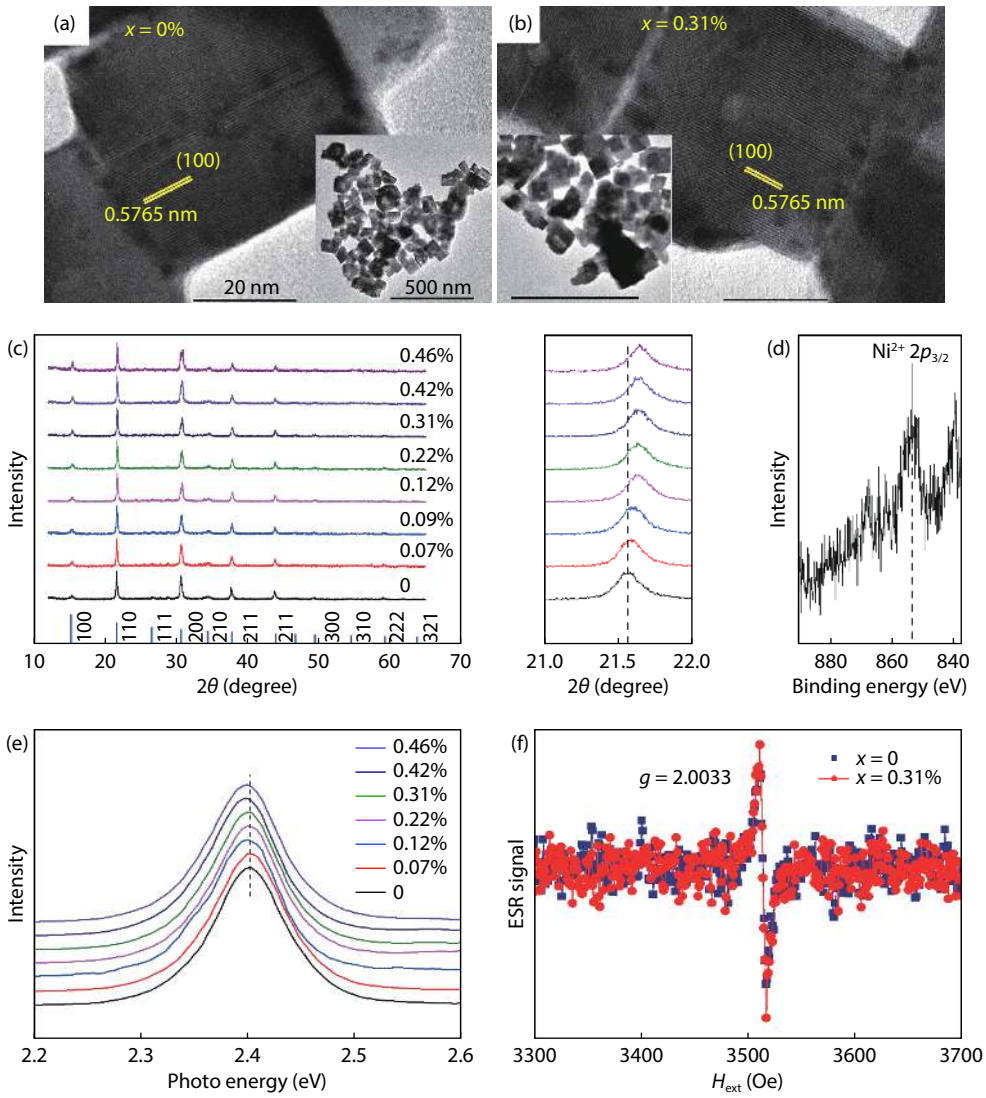

Fig. 1. (Color online) Crystal and electronic structure characterizations. High-resolution TEM images of $CsPb_{1-x}Ni_xBr_3$ nanocrystals with (a) $x = 0$ and (b) $x = 0.31\%$. The insets show corresponding low-resolution TEM images. (c) XRD patterns of $CsPb_{1-x}Ni_xBr_3$ nanocrystals with variant x values. The bottom blue vertical lines index the XRD patterns of $CsPbBr_3$ with a cubic-phase structure (PDF#54-0752). The enlarged view of the XRD spectra near $2\theta = 21.5°$ is also shown. (d) X-ray photoelectron spectroscopy of the Ni $2p$ level in $CsPb_{1-x}Ni_xBr_3$ with $x = 0.31\%$. (e) Photoluminescence spectra of RT-synthesized $CsPb_{1-x}Ni_xBr_3$ nanocrystals with different x, measured at 300 K. (f) The ESR spectra of $CsPb_{1-x}Ni_xBr_3$ nanocrystals with $x = 0$ and 0.31%, measured at 300 K. 1 Oe = 0.1 mT. All samples used here were RT-synthesized.

tions. As for defective $CsPbBr_3$ (right-hand column), a Br atom (indicated by the blue arrow) was removed from the perfect supercell to create a V_{Br}, and the lattice was then fully relaxed to a stable state for study; see Experimental section for calculation details. Fig. 2(b) displays the slice of deformation charge density (DCD) of the Pb–Br layer from the $CsPbBr_3$ (200) plane, without and with V_{Br}. This permits us to study the effects of V_{Br} on charge transfer after forming chemical bonds. The Pb–Br bonds showed ionic character, where the Br atoms gained electrons and the Pb atoms contributed electrons. The charge density distribution in perfect $CsPbBr_3$ was highly symmetric. When V_{Br} was introduced, it became asymmetric, particularly in the vicinity of V_{Br}. The V_{Br} site exhibited a charge-accumulation environment, indicating that there was strong bonding between the Pb atoms around V_{Br}.

To study whether or not the charge distribution asymmetry could induce magnetic states, calculations on spin-resolved density of states (DOSs) were carried out; the results are shown in Fig. 2(c). As expected, the total DOSs of the perfect $CsPbBr_3$ showed high spin-degeneracy, that is, the distribution of the spin-up and spin-down electrons was completely symmetrical, indicating the nonmagnetic nature of perfect $CsPbBr_3$. The total DOSs of the perfect $CsPbBr_3$ were discrete and sharp, revealing that the electronic states were rather localized. No states were present inside the bandgap of perfect $CsPbBr_3$. Regarding defective $CsPbBr_3$, clear spin splitting can be seen from its total DOSs (*i.e.*, the spin degeneracy has lifted). The magnitude of the spin splitting near the valence band maximum was ~ 38 meV. The net magnetic moment of the defective supercell was calculated to be $6\mu_B$. Moreover, the defective $CsPbBr_3$ exhibited extended DOSs, indicating that the electronic states in defective $CsPbBr_3$ were much more delocalized than those in perfect $CsPbBr_3$. Particularly, some impurity states were present inside the bandgap of defective $CsPbBr_3$. Analysis of the partial DOSs of the defective $CsPbBr_3$ revealed that: (1) the conduction band consisted of Pb $6p$ orbitals (predominant) and Br $4s$ and $4p$ orbitals; (2) the valence bands were formed by Br $4p$ orbitals (predomin-

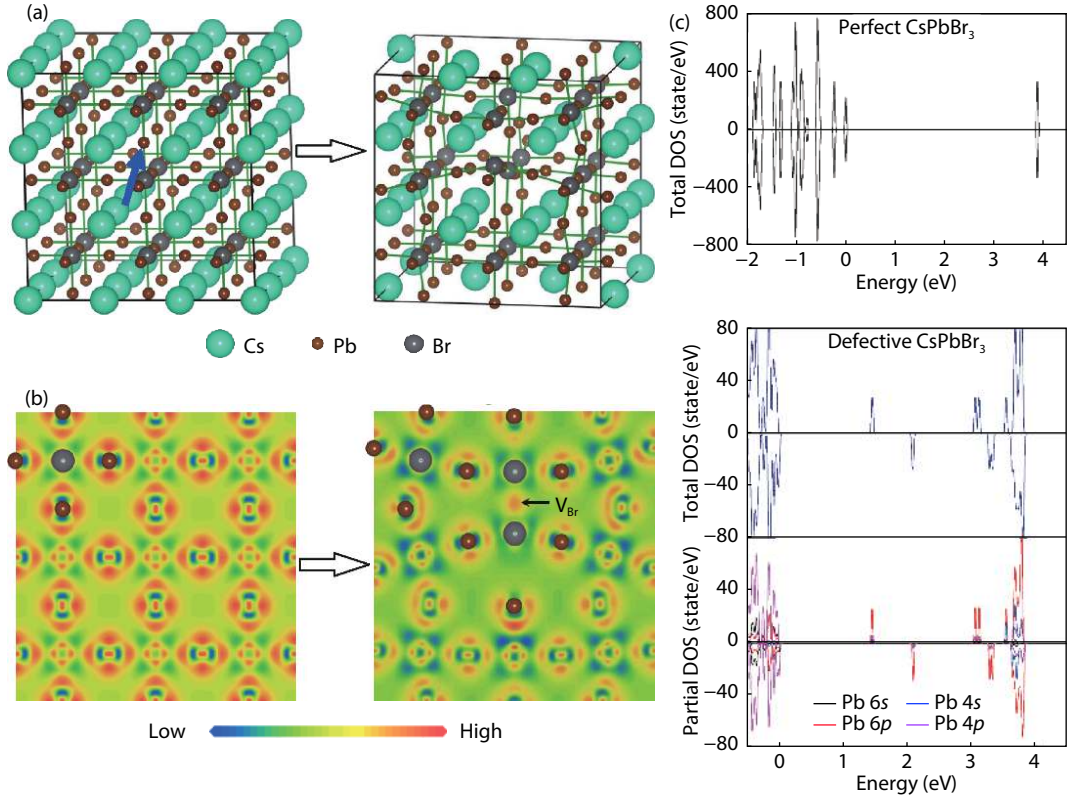

Fig. 2. (Color online) First-principle calculations. (a) The 3 × 3 × 3 $CsPbBr_3$ supercells used in DFT calculations. Left: perfect lattice, where the Br atom indicated by the blue arrow will be removed to create a V_{Br}. Right: relaxed lattice with the presence of a V_{Br}. (b) DCD of the perfect (left) and defective (right) $CsPbBr_3$. High (low) charge density corresponds to charge accumulation (depletion) regimes. (c) Spin-resolved total and partial DOSs of the perfect and defective $CsPbBr_3$ supercells.

ant) and Pb 6*s* and 6*p* orbitals; (3) Pb 6*s* and 6*p* orbitals exhibited strong hybridization with Br 4*s* and 4*p* orbitals; and (4) the impurity states were mainly composed of Pb 6*p* orbitals, whereas the Br 4*p* orbital also contributed a small part of the impurity states, due to its hybridization with the Pb 6*p* orbital. The exchange interaction between vacancies was studied by calculating the total energy of a 3 × 3 × 3 $CsPbBr_3$ supercell containing two V_{Br} and comparing the energy for the ferromagnetic (E_{FM}) and antiferromagnetic (E_{AFM}) states. It was found that E_{FM} was lower than E_{AFM}, with an energy of 3.73 meV, suggesting that the bivacancy system had a ferromagnetic ground state.

3.3. Experimental demonstration of vacancy-induced ferromagnetism

In experiment, we measured the magnetic properties of a number of LHPs including pure $CsPbCl_3$, $CsPbBr_3$, $CsPbI_3$, and $CH_3NH_3PbBr_3$, using a vibrating sample magnetometer (see Experimental section). Fig. 3(a) displays the magnetization versus H_{ex} curves of RT-synthesized $CsPbBr_3$ nanocrystals at measuring temperatures of 4, 100, 200, 300, and 400 K. The linear diamagnetic backgrounds have already been subtracted. All curves show a clear ferromagnetic behavior with S-shape signals. That is, the magnetization increased with H_{ex} before then becoming saturated at a certain H_{ex} value. The curves show little or no hysteresis (inset of Fig. 3(a)), and the saturation magnetization (M_s) does not change much with temperature (Fig. 3(b)), features of d^0 ferromagnetism[38, 39]. The ferromagnetic behaviors observed at low temperatures persisted as the temperature rose to 400 K, suggesting that the Curie temperature of the $CsPbBr_3$ nanocrystals is above 400 K.

Moreover, as shown in Fig. 3(c), the ferromagnetism of the $CsPbBr_3$ nanocrystal could be tuned by treating the nanocrystal surfaces with oleylammonium bromide (OAmBr): the M_s decreased from 0.99 memu/g before the treatment to 0.57 memu/g after the treatment. We also studied the magnetic properties of $CsPbBr_3$ quantum dots synthesized by hot injection at 170 °C and $CsPbBr_3$ single crystals (see Experimental section for synthesis details). We found that both samples only showed diamagnetic background signals at 300 K (Fig. S1, Supporting Information), which indicates that they were nonmagnetic at 300 K. Surface treatment with OAmBr can passivate the V_{Br} and thus decrease V_{Br} concentration near the surfaces. Hot-injection synthesized and single-crystal $CsPbBr_3$ also have reduced V_{Br}, as indicated by our ESR measurements (Fig. S2, Supporting Information). Together with the first-principle calculation results, the magnetic results of the surface-passivation and high-quality $CsPbBr_3$ samples confirmed the V_{Br} origin of the ferromagnetism observed in the RT-synthesized $CsPbBr_3$ nanocrystals.

Figs. 3(d)–3(f) present the magnetic properties of RT-synthesized tetragonal-phase $CsPbCl_3$, orthorhombic-phase $CsPbI_3$, and cubic-phase $CH_3NH_3PbBr_3$ (structure and optical characterizations are shown in Fig. S3, Supporting Information), respectively. They all exhibited clear d^0 ferromagnetism at 300 K, and surface passivation suppressed it. Moreover, similar to the case of $CsPbBr_3$, no ferromagnetism was observed in the hot-injection synthetized $CsPbCl_3$, $CsPbI_3$, and $CH_3NH_3PbBr_3$ at a measuring temperature of 300 K (Fig. S4, Supporting Information). Accordingly, we conclude that va-

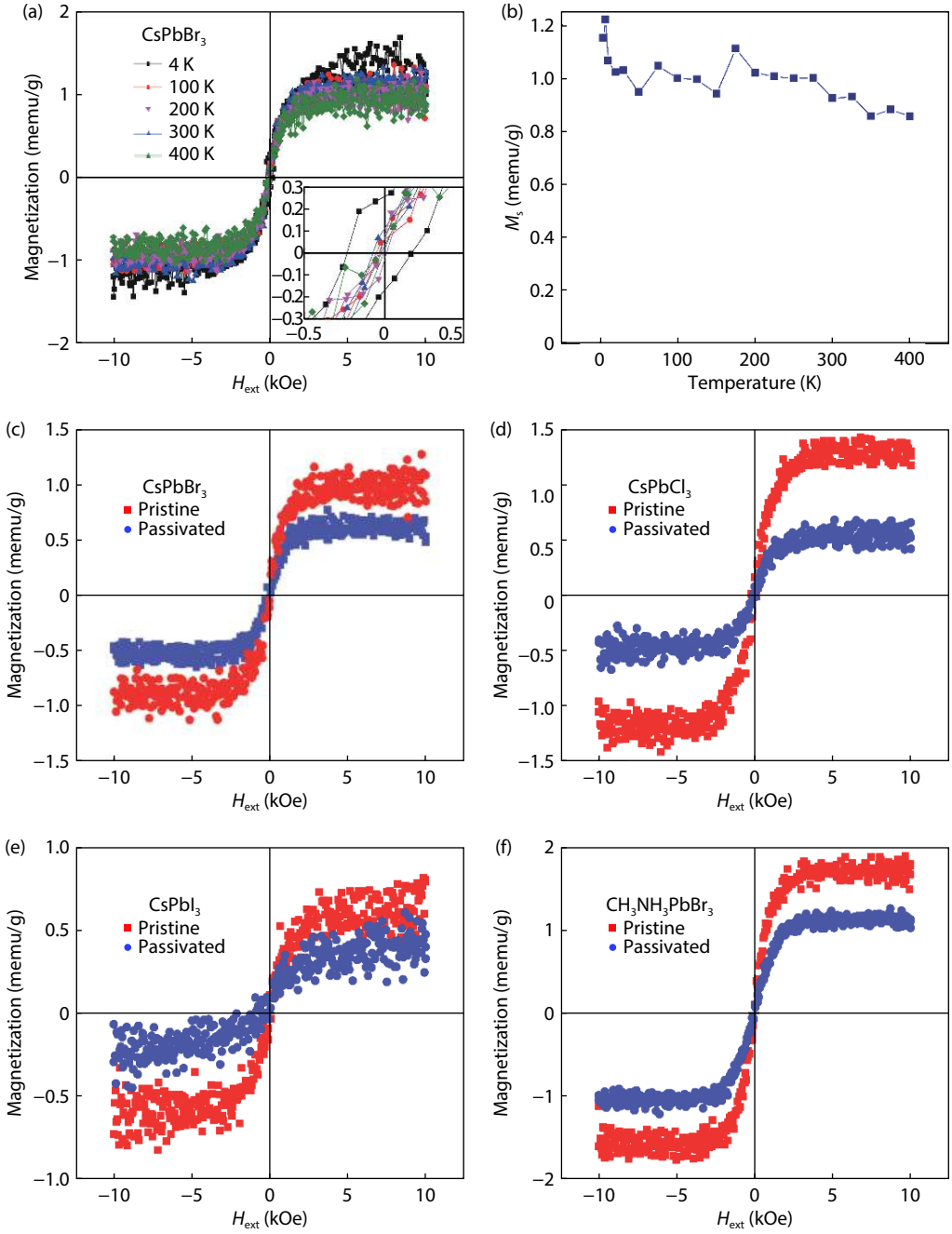

Fig. 3. (Color online) Magnetic properties of RT-synthesized LHPs. (a) Magnetization versus H_{ext} curves of RT-synthesized pure $CsPbBr_3$ nanocrystals measured at several representative temperatures. The diamagnetic signals have already been subtracted. Inset shows the enlarged view of low field regimes between ±0.5 kOe. (b) Temperature dependence of M_s of pure $CsPbBr_3$ nanocrystals. Effects of (c) OAmBr passivation, (d) OAmCl passivation, (e) OAmI passivation, and (f) OAmBr passivation on the ferromagnetism of $CsPbBr_3$, $CsPbCl_3$, $CsPbI_3$, and $CH_3NH_3PbBr_3$, respectively, measured at 300 K.

cancy-induced d^0 ferromagnetism should be universal in LHP materials.

3.4. Ferromagnetism enhancement with 3*d* ion doping

For practical device applications, the ferromagnetism should be as strong as possible, to stabilize the spins against external thermal fluctuations. As it has a defect-origin nature, d^0 ferromagnetism can in principle be enhanced by increasing the defect concentration. However, having too many vacancies in LHPs is potentially hazardous to their structural stability, due to the vacancy-mediated ionic migration effect[40], a tough issue that remains to be solved. Recently, doping LHPs with TM ions has been shown to improve both the optical properties and structural stability of LHPs[41]. Therefore, we attempted to dope the RT-synthesized $CsPbBr_3$ nanocrystals with 3*d* TM ions, and studied whether this could enhance the d^0 ferromagnetism.

Fig. 4(a) presents the magnetization versus H_{ex} curves of RT-synthesized $CsPbBr_3$ nanocrystals doped with Mn, Fe, Co, Ni, Cu, and Zn, measured at 300 K (The XRD study confirmed the successful incorporation of these 3*d* dopants into the Pb site; see Fig. S5, Supporting Information). Even a tiny fraction (< 1%) of 3*d* dopants led to a significant modulation of the ferromagnetism of the $CsPbBr_3$ nanocrystals. Compared with pure $CsPbBr_3$, as shown in Fig. 4(b), doping with 0.54% Fe,

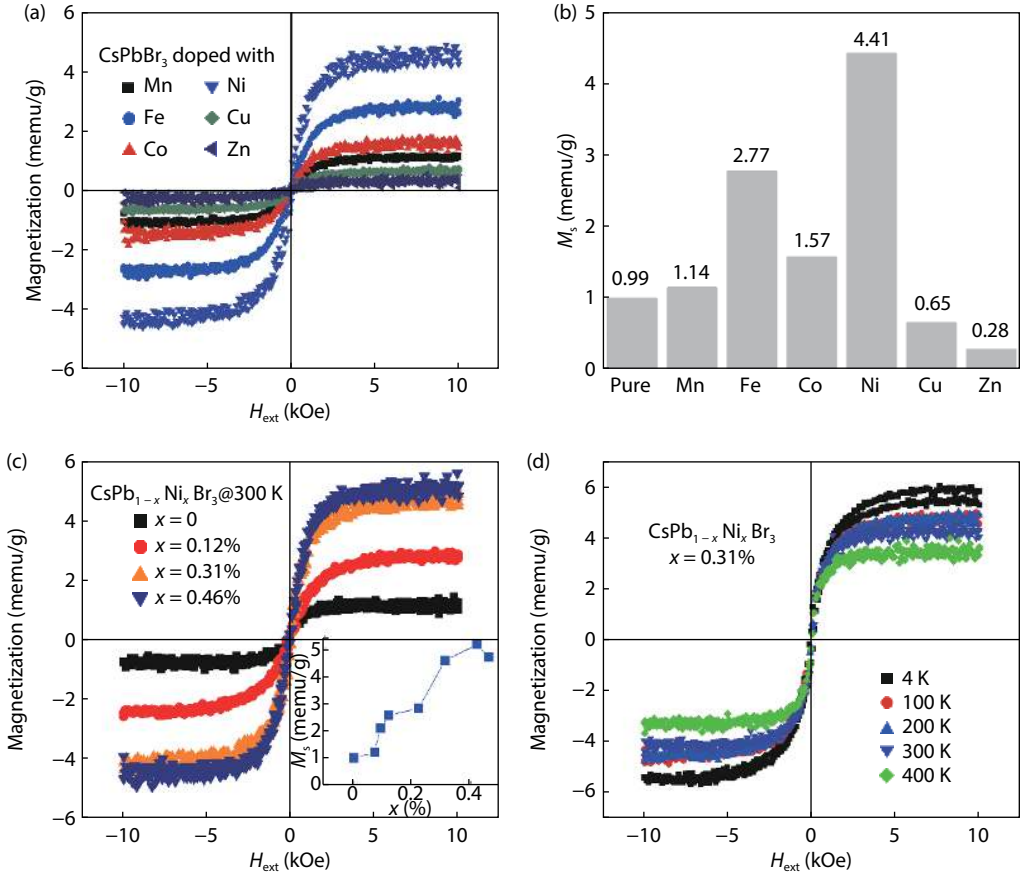

Fig. 4. (Color online) 3*d* dopant effects on the magnetic properties of $CsPbBr_3$. (a) Magnetization versus H_{ext} curves of RT-synthesized $CsPbBr_3$ nanocrystals doped with 1.7% Mn, 0.54% Fe, 0.87% Co, 0.31% Ni, 0.35% Cu, and 0.86% Zn, measured at 300 K. (b) M_s of the magnetization curves presented in (a). (c) Magnetization versus H_{ext} curves of RT-synthesized $CsPb_{1-x}Ni_xBr_3$ nanocrystals with x = 0, 0.12%, 0.31%, and 0.46%, measured at 300 K. Inset shows the x dependence of M_s. (d) Magnetization versus H_{ext} curves of RT-synthesized $CsPb_{1-x}Ni_xBr_3$ nanocrystals with x = 0.31% at measuring temperatures of 4, 100, 200, 300, and 400 K. The diamagnetic signals have already been subtracted.

0.87% Co, and 0.31% Ni enhanced the M_s by a factor of three, two, and four, respectively, while doping with 0.35% Cu and 0.86% Zn impaired the M_s. The remarkable variation of the M_s indicates that the exchange coupling is sensitive to 3*d* ions doped, which have variable electron configuration in the 3*d* orbitals. As a representative, Fig. 4(c) shows the Ni^{2+} dopant concentration dependence of magnetic properties in $CsPb_{1-x}Ni_xBr_3$ (see Fig. 1 for structural characterizations). The M_s roughly increased as increased from 0 to 0.46% (inset of Fig. 4(c)). Due to solubility limitation, we were unable to investigate the effects of higher x on the M_s. Fig. 4(d) displays the magnetization curves of $CsPb_{1-x}Ni_xBr_3$ with x = 0.31% at measuring temperatures of 4, 100, 200, 300, and 400 K. In contrast to pure $CsPbBr_3$, where the M_s did not vary significantly with temperature (Figs. 3(a) and 3(b)), the M_s of Ni-doped $CsPbBr_3$ exhibited strong temperature dependence behavior: it decreased by approximately 42% as the temperature increased from 4 to 400 K. Nevertheless, all of the magnetization curves presented in Figs. 4(c) and 4(d) showed little or no hysteresis, indicating that the ferromagnetism of Ni-doped $CsPbBr_3$ should also originate from V_{Br} – the same as for pure $CsPbBr_3$. The dramatic temperature dependence of the M_s reflects that there was strong coupling between the V_{Br} and Ni^{2+} dopants. Only paramagnetism was found in the hot-injection-synthesized Ni-doped $CsPbBr_3$ quantum dots (Fig. S6, Supporting Information), further confirming the V_{Br} origin of the ferromagnetism.

4. Discussions

Here we discuss V_{Br}-induced ferromagnetism and its enhancement with 3*d* dopants in an exchange coupling mechanism based on a magnetic polaron model[42, 43], which is depicted in Fig. 5. A magnetic polaron is a phonon cloud carrying net spin moments, and it usually appears with the formation of a vacancy defect[41]. As mentioned above, V_{Br} in $CsPbBr_3$ is a shallow donor defect. This means that the magnetic polaron associated with a particular V_{Br} is confined in a hydrogenic orbital with a diameter $D = 2\varepsilon(m/m^*)a_0$, where ε is the high-frequency dielectric constant, m is the electron mass, m^* is the effective mass of the donor electron, and a_0 is the Bohr radius (~0.053 nm). Using ε = 4.3 and m/m^* = 6.71[44], the D value of a magnetic polaron in $CsPbBr_3$ was calculated to be 3.06 nm, which can extend to a distance corresponding to 5.2 unit cells of cubic-phase $CsPbBr_3$. By virtue of this large size, magnetic polarons in $CsPbBr_3$ are prone to overlap with each other, and the exchange coupling between them aligns the spin moments of V_{Br}[42, 43], leading to the long-range ferromagnetic ordering observed in the defective $CsPbBr_3$ nanocrystals. When Ni^{2+} ions are introduced and fall into the magnetic polarons, they can interact with V_{Br} via exchange coupling, because the Ni^{2+} ion has an open $3d^8$ subshell where the e_g level is partially filled. As the 3*d* orbital has a stronger exchange coupling constant than the *s* and *p* orbitals, the exchange coupling strength between the magnetic polarons

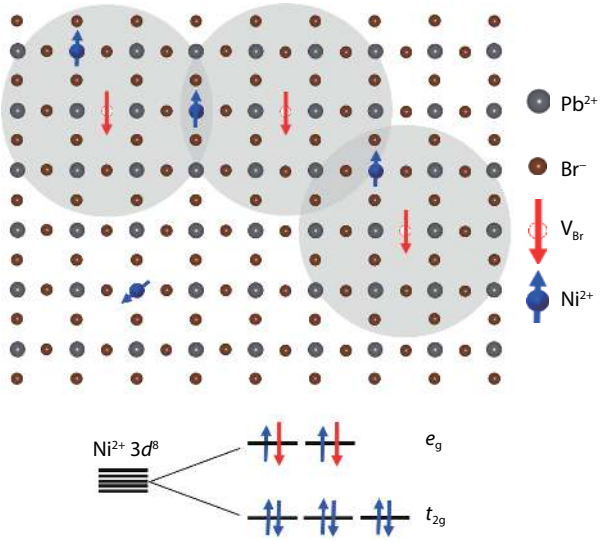

Fig. 5. (Color online) Schematic of vacancy-induced ferromagnetism. A donor electron associated with a V_{Br} polarizes the surrounding lattices within its hydrogenic orbital, leading to the formation of a magnetic polaron (gray circles). Due to the shallow nature of the V_{Br}, the magnetic polarons have extended wave functions. As a result, the overlap of the magnetic polarons aligns the spins of the V_{Br} (red arrows) via exchange coupling, producing long-range spin ordering (*i.e.*, ferromagnetism). Regarding a Ni^{2+} ion with a $3d^8$ subshell, the only unoccupied 3*d* orbitals available are in the e_g level. Therefore, the exchange coupling between the Ni^{2+} spins (blue arrows) and the V_{Br} spins is antiferromagnetic. Nonetheless, the exchange coupling between two V_{Br} mediated by a same Ni^{2+} ion is ferromagnetic. Note here that the Cs ions are not shown, and that the sizes of the magnetic polarons are not scaled to their calculated values (see the Discussion section of the main text).

can be enhanced through Ni^{2+}-mediated interactions, leading to the enhancement of ferromagnetism in doped $CsPbBr_3$ nanocrystals. Obviously, ferromagnetism will increase with increasing dopant concentration, as observed in Fig. 4(c). As for Zn dopants, the Zn^{2+} ion has a fully-filled $3d^{10}$ subshell, which has no exchange coupling with the magnetic polaron, and thus did not enhance ferromagnetism (Fig. 4(b)). Regarding the cases of the surface passivation, the hot-injection prepared LHP quantum dots and the single crystals, decreases in V_{Br} concentration will increase the distance between the spins of V_{Br}, and thus weaken the exchange coupling strength between the magnetic polarons, explaining the lack of ferromagnetism in them.

It is worthy to point out that, because of the large magnetic polarons, even a very low doping level of Ni^{2+} ions (up to 0.46%) can lead to the significant enhancement of the RT ferromagnetism in $CsPbBr_3$. In contrast, previously widely studied oxide semiconductors had much smaller magnetic polaron than $CsPbBr_3$; the *D* values for ZnO, TiO_2, and SnO_2 were 1.52, 0.96, and 1.72 nm, respectively[43]. As a result, a much higher doping level of 3*d* ions (usually above 3%) was required to modulate the ferromagnetism. High-level doping may cause segregation of 3*d* ions, which puzzled the origin of ferromagnetism in previous dilute ferromagnetic oxide semiconductors[45]. The ability of the modulation of the ferromagnetism at low-level doping indicates that the LHP materials should be an idea platform for further theoretical and experimental studies aiming at clarifying the relationship between ferromagnetism, lattice defects, and exotic dopants.

5. Conclusions

In summary, we have reported a universal observation of vacancy-induced ferromagnetism in nominally nonmagnetic LHP semiconductors, including $CsPbCl_3$, $CsPbBr_3$, $CsPbI_3$, and $CH_3NH_3PbBr_3$. We have documented that this phenomenon is stable at temperatures well above 300 K, and that it is enhanced by doping LHPs with 3*d* ions. Our first-principle calculations suggest that the vacancy-induced ferromagnetism arises from spin-splitting states produced by halide vacancy. Our results are expounded within an exchange-coupled magnetic polaron model, and provide new physical insights for comprehensive understanding of defect physics in LHPs. Given that growth-related vacancies in LHP materials are unavoidable, making use of the vacancy-induced ferromagnetic properties will extend the functionalities of LHP-based devices, for example, for spintronic applications in spin light-emitting diodes and spin transistors. It would also be interesting to study more dopants, such as 4*d* TM ions and 4*f* rare-earth metal ions, and investigate whether they can lead to an even stronger ferromagnetism in LHPs, which would be crucial for practical applications.

Acknowledgements

Z. Sun and B. Cai contributed equally to this work. This work was financially supported by NSFC (61725402) and the Natural Science Foundation of Jiangsu Province (BK20190475).

References

[1] Žutić I, Fabian J, Das Sarma S. Spintronics: Fundamentals and applications. Rev Mod Phys, 2004, 76, 323
[2] Qi B, Ólafsson S, Gíslason H P. Vacancy defect-induced d0 ferromagnetism in undoped ZnO nanostructures: Controversial origin and challenges. Prog Mater Sci, 2017, 90, 45
[3] Matsumoto Y, Murakami M, Shono T, et al. Room-temperature ferromagnetism in transparent transition metal-doped titanium dioxide. Science, 2001, 291, 854
[4] Sharma P, Gupta A, Rao K V, et al. Ferromagnetism above room temperature in bulk and transparent thin films of Mn-doped ZnO. Nat Mater, 2003, 2, 673
[5] Ogale S B, Choudhary R J, Buban J, et al. High temperature ferromagnetism with a giant magnetic moment in transparent Co-doped $SnO_{2-\delta}$. Phys Rev Lett, 2003, 91, 077205
[6] Fernandes V, Klein J J, Mattoso N, et al. Room temperature ferromagnetism in Co-doped CeO_2 films on Si(001). Phys Rev B, 2007, 75, 121304(R)
[7] Reed M L, El-Masry N A, Stadelmaier H H, et al. Room temperature ferromagnetic properties of (Ga, Mn)N. Appl Phys Lett, 2001, 79, 3473
[8] Coey J M D. d^0 Ferromagnetism. Solid State Sci, 2005, 7, 660
[9] Sundaresan A, Bhargavi R, Rangarajan N, et al. Ferromagnetism as a universal feature of nanoparticles of the otherwise nonmagnetic oxides. Phys Rev B, 2006, 74, 161306
[10] Rumaiz A K, Ali B, Ceylan A, et al. Experimental studies on vacancy induced ferromagnetism in undoped TiO_2. Solid State Commun, 2007, 144, 334
[11] Zhan P, Wang W P, Liu C, et al. Oxygen vacancy–induced ferromagnetism in un-doped ZnO thin films. J Appl Phys, 2012, 111, 033501
[12] Niu G, Hildebrandt E, Schubert M A, et al. Oxygen vacancy in-

duced room temperature ferromagnetism in Pr-doped CeO_2 thin films on silicon. ACS Appl Mater Interfaces, 2014, 6, 17496

[13] Roul B, Rajpalke M K, Bhat T N, et al. Experimental evidence of Ga-vacancy induced room temperature ferromagnetic behavior in GaN films. Appl Phys Lett, 2011, 99, 162512

[14] Wang H X, Zong Z C, Yan Y. Mechanism of multi-defect induced ferromagnetism in undoped rutile TiO_2. J Appl Phys, 2014, 115, 233909

[15] Han X P, Lee J, Yoo H I. Oxygen-vacancy-induced ferromagnetism in CeO_2 from first principles. Phys Rev B, 2009, 79, 100403

[16] Dev P, Xue Y, Zhang P H. Defect-Induced intrinsic magnetism in wide-gap III nitrides. Phys Rev Lett, 2008, 100, 117204

[17] Wang Y R, Piao J Y, Xing G Z, et al. Zn vacancy induced ferromagnetism in K doped ZnO. J Mater Chem C, 2015, 3, 11953

[18] Ahn C H, Kim Y Y, Kim D C, et al. Erratum: "A comparative analysis of deep level emission in ZnO layers deposited by various methods " [J. Appl. Phys. 105, 013502 (2009)]. J Appl Phys, 2009, 105, 089902

[19] Fabbri F, Villani M, Catellani A, et al. Zn vacancy induced green luminescence on non-polar surfaces in ZnO nanostructures. Sci Rep, 2014, 4, 5158

[20] Morgan B J, Watson G W. Polaronic trapping of electrons and holes by native defects in anatase TiO_2. Phys Rev B, 2009, 80, 233102

[21] Lyons J L, van de Walle C G. Computationally predicted energies and properties of defects in GaN. npj Comput Mater, 2017, 3, 12

[22] Akkerman Q A, Rainò G, Kovalenko M V, et al. Genesis, challenges and opportunities for colloidal lead halide perovskite nanocrystals. Nat Mater, 2018, 17, 394

[23] Walsh A, Scanlon D O, Chen S Y, et al. Self-regulation mechanism for charged point defects in hybrid halide perovskites. Angew Chem Int Ed, 2015, 54, 1791

[24] Dong Q F, Fang Y J, Shao Y C, et al. Solar cells. Electron-hole diffusion lengths > 175 μm in solution-grown $CH_3NH_3PbI_3$ single crystals. Science, 2015, 347, 967

[25] Dutta A, Behera R K, Pal P, et al. Near-unity photoluminescence quantum efficiency for all $CsPbX_3$ (X = Cl, Br, and I) perovskite nanocrystals: A generic synthesis approach. Angew Chem Int Ed, 2019, 58, 5552

[26] Jeon N J, Na H, Jung E H, et al. A fluorene-terminated hole-transporting material for highly efficient and stable perovskite solar cells. Nat Energy, 2018, 3, 682

[27] Lin K, Xing J, Quan L N, et al. Perovskite light-emitting diodes with external quantum efficiency exceeding 20 per cent. Nature, 2018, 562, 245

[28] Cao Y, Wang N N, Tian H, et al. Perovskite light-emitting diodes based on spontaneously formed submicrometre-scale structures. Nature, 2018, 562, 249

[29] Yin W J, Shi T T, Yan Y F. Unusual defect physics in $CH_3NH_3PbI_3$ perovskite solar cell absorber. Appl Phys Lett, 2014, 104, 063903

[30] Kang J, Wang L W. High defect tolerance in lead halide perovskite $CsPbBr_3$. J Phys Chem Lett, 2017, 8, 489

[31] Zhai Y X, Baniya S, Zhang C, et al. Giant Rashba splitting in 2D organic-inorganic halide perovskites measured by transient spectroscopies. Sci Adv, 2017, 3, e1700704

[32] Zhang C, Sun D L, Yu Z G, et al. Field-induced spin splitting and anomalous photoluminescence circular polarization in $CH_3NH_3PbI_3$ films at high magnetic field. Phys Rev B, 2018, 97, 134412

[33] Sun D L, Zhang C, Kavand M, et al. Surface-enhanced spin current to charge current conversion efficiency in $CH_3NH_3PbBr_3$-based devices. J Chem Phys, 2019, 151, 174709

[34] Wang J, Zhang C, Liu H, et al. Spin-optoelectronic devices based on hybrid organic-inorganic trihalide perovskites. Nat Commun, 2019, 10, 129

[35] Kresse, Furthmüller. Efficient iterative schemes for ab initio total-energy calculations using a plane-wave basis set. Phys Rev B, 1996, 54, 11169

[36] Perdew J P, Ruzsinszky A, Csonka G I, et al. Restoring the density-gradient expansion for exchange in solids and surfaces. Phys Rev Lett, 2008, 100, 136406

[37] Jakes P, Zimmermann J, von Seggern H, et al. Eu^{2+}-doped CsBr photostimulable X-ray storage phosphors: Analysis of defect structure by high-frequency EPR. Funct Mater Lett, 2014, 7, 1350073

[38] Coey M, Ackland K, Venkatesan M, et al. Collective magnetic response of CeO_2 nanoparticles. Nat Phys, 2016, 12, 694

[39] Coey J M D. Magnetism in d^0 oxides. Nat Mater, 2019, 18, 652

[40] Yuan Y B, Huang J S. Ion migration in organometal trihalide perovskite and its impact on photovoltaic efficiency and stability. Acc Chem Res, 2016, 49, 286

[41] Yong Z J, Guo S Q, Ma J P, et al. Doping-enhanced short-range order of perovskite nanocrystals for near-unity violet luminescence quantum yield. J Am Chem Soc, 2018, 140, 9942

[42] Kaminski A, Das Sarma S. Polaron percolation in diluted magnetic semiconductors. Phys Rev Lett, 2002, 88, 247202

[43] Coey J M D, Venkatesan M, Fitzgerald C B. Donor impurity band exchange in dilute ferromagnetic oxides. Nat Mater, 2005, 4, 173

[44] Kang Y, Han S. Intrinsic carrier mobility of cesium lead halide perovskites. Phys Rev Appl, 2018, 10, 044013

[45] Pan F, Song C, Liu X J, et al. Ferromagnetism and possible application in spintronics of transition-metal-doped ZnO films. Mater Sci Eng R, 2008, 62, 1